Analysis of active alignment control of the Hobby-Eberly Telescope wide-field corrector using Shack-Hartmann wavefront sensors

Lee, Hanshin, Hart, Michael, Hill, Gary, Rafal, M.

Hanshin Lee, Michael Hart, Gary J. Hill, M. D. Rafal, "Analysis of active alignment control of the Hobby-Eberly Telescope wide-field corrector using Shack-Hartmann wavefront sensors," Proc. SPIE 7738, Modeling, Systems Engineering, and Project Management for Astronomy IV, 77380I (4 August 2010); doi: 10.1117/12.857121

SPIE.

Event: SPIE Astronomical Telescopes + Instrumentation, 2010, San Diego, California, United States

Analysis of active alignment control of the Hobby-Eberly Telescope* Wide Field Corrector using Shack-Hartmann wavefront sensors

Hanshin Lee [a,†], Michael Hart[b], Gary J. Hill[a], and M. D. Rafal[a]

[a] McDonald Observatory, University of Texas at Austin, 1 University Station C1402, Austin, TX 78712-0259, USA

[b] Hart Scientific Consulting International L.L.C., E. Burns St., Tucson, AZ 85711, USA

ABSTRACT

One of the key aspects of the Wide-Field Upgrade (WFU) for the 10m Hobby-Eberly Telescope (HET) is the use of wavefront sensing (WFS) to close the loop of active alignment control of the new four-mirror Wide-Field Corrector (WFC), as it tracks sidereal motion, with respect to the fixed spherical segmented primary mirror. This makes the telescope pupil dynamically change in shape. This is a unique challenge to the WFS on the HET, in addition to various influences of seeing, primary mirror segment errors, and dynamic deflection of the internal optical components of the WFC. We conducted extensive simulations to understand the robustness of the WFS in the face of these errors and the results of these analyses are discussed in this paper.

Keywords: Wavefront sensing, Shack-Hartmann wavefront sensor, Hobby-Eberly Telescope, HETDEX

1. INTRODUCTION

In the next two years, the Hobby-Eberly Telescope (HET) will be upgraded with a 22-arcmin. diameter field of view wide field corrector (WFC), a new tracker and prime focus instrument package (PFIP), and new metrology systems to support the Hobby-Eberly Dark Energy Experiment (HETDEX)[1-2]. The new corrector has improved image quality and a 10 m pupil diameter. The periphery of the field (i.e. an annular field from 18′ to 22′ diameter, called the metrology service field) will be used for guiding and wavefront sensing to provide the necessary feedback to keep the telescope correctly aligned. The WFC will give 30 times larger observing area than the current HET corrector. It is a four-mirror design with two concave 1meter diameter mirrors, one concave 0.9meter diameter mirror, and one convex 0.24meter diameter mirror. The corrector is designed for feeding optical fibers at f/3.65 to minimize focal ratio degradation, and so the chief ray from all field angles is normal to the focal surface. This is achieved with a concave spherical focal surface centered on the exit pupil. The imaging performance is 0.5arcsec or better over the entire 22arcmin field of view, and vignetting is minimal. As in the current HET, the WFC will track sidereal motion with respect to the optical axis of the fixed spherical primary (M1). Thus, the WFC needs to be continuously positioned to maintain its alignment in order to deliver required image quality. This demands constant monitoring and updating of the position of its components. Table 1 shows the required ranges of misalignments of the WFC as a rigid body at any given track position.

Table 1. The required ranges of misalignments of the WFC.

Alignment parameters	Decenter	Defocus	Tip/tilt	Rho
Accuracy[peak-to-peak]	±10 μm	±10 μm	±4 arcsec.	±20 arcsec.

The feedback to keep these alignment specifications requires robust metrology and we plan to deploy the following metrology subsystems[3] for this:

- Guide probes (GP): Monitoring the position on the sky, and plate scale of the optical system, and monitor the image quality and atmospheric transparency.
- Wavefront sensors (WS): Monitoring the plate-scale, focus, and tilt of the WFC.
- Distance measuring interferometer (DMI): Monitoring the physical distance between the WFC and primary mirror.

* The Hobby – Eberly Telescope is operated by McDonald Observatory on behalf of the University of Texas at Austin, the Pennsylvania State University, Stanford University, Ludwig-Maximillians-Universität München,and Georg-August-Universität, Göttingen

† Hanshin Lee.: E-mail: lee@astro.as.utexas.edu

Modeling, Systems Engineering, and Project Management for Astronomy IV,
edited by George Z. Angeli, Philippe Dierickx, Proc. of SPIE Vol. 7738, 77380I
 · doi: 10.1117/12.857121

- Tip-tilt sensor (TTS): Monitoring the physical tip/tilt of the WFC with respect to the optical axis of the primary mirror.

Among the above metrology sub-systems, the WS is a newly introduced system to the HET in order to close the loop on all axes of the system (together with the DMI and TTS adapted from the current tracker metrology system[4]). These systems can provide sufficient redundancy in order to obtain the highest possible reliability in monitoring the alignment of the WFC. DMI and TTS measurements are directly related to the alignment state of the mechanical structure of the WFC, while responses from the WS are analyzed to determine the "*optical*" alignment state of the WFC. The WS analysis is based on the following alignment–aberration relations. Decenters of the WFC causes systematic wavefront tilts across the field. This is equivalent to the telescope pointing error and equivalent to the stellar position measurement from the GP. Tilt errors add field constant coma to the aberration field of the WFC, while the axial motion introduces defocus aberration that is also field constant. The defocus aberration, however, can also be produced when the global radius of curvature (GRoC) of M1 changes. As this variation can also produce plate scale variation, an appropriate monitoring system is necessary. Although the segment alignment maintenance system (SAMS)[5] maintains the positions of the 91 mirror segments with respect to each other, it is less sensitive to the global radius of curvature of M1. The GRoC is to be monitored by the combination of focus position from the WS with the physical measurement from the DMI and checked by the plate scale measured from the positions of guide stars on the GP. The feedback from the SAMS can be used as a redundant piece of information on the GRoC.

A unique challenge is presented by the nature of the HET: the fixed M1 and tracking WFC cause substantial changes in the pupil illumination over the course of an observation. In addition, M1 consists of 91 hexagonal segments with inevitable non-zero error variances in their pointing and radii of curvature. The segments are also un-phased and show astigmatic surface figure error. To investigate the feasibility of the WFS-based active alignment control of the HET in the face of these challenges, we have developed a comprehensive model for the telescope, WFC, and WFS and performed extensive analyses as described in the following sections. In Section 2, we details the models used in the WFS simulations. The simulation results are discussed in Section 3. The plan for test, calibration, and construction of the WS is summarized in Section 4.

2. DESCRIPTIONS OF WFS SIMULATION

2.1 Shack-Hartmann wavefront sensor design parameters.

The primary function of the WFS is to sense the aberrations given by the WFC's rigid-body misalignment with respect to the fixed M1, thereby providing necessary alignment corrections for nullifying the alignment-driven aberrations. When the internal optical elements of the WFC are in perfect alignment, the WFC misalignment is equivalent to the secondary mirror misalignment in a two-mirror telescope system. Thus, the WFC develops similar alignment-driven aberrations to those in a two-mirror telescope: field constant wavefront tip/tilt (Z_2 and Z_3) due to decenter (x_d, y_d), defocus (Z_4) due to axial motion (z_d), and coma aberrations (Z_7 and Z_8) due to tip/tilt motions (x_t, y_t), where Z_i is the i-th standard Zernike polynomial coefficient. In addition, the rotation about the optical axis (z_r) can shift the stellar image with respect to the sensor, which will be seen as wavefront tip/tilt. Also, a variation in the global radius of curvature of M1 (Δ_{GRoC}) can radially shift the stellar image and add defocus aberration[6]. Virtually no linear field astigmatism and curvature is introduced by the WFC misalignment. In reality, however, there will be small amounts of misalignment of the internal WFC mirrors due to change in gravity vector and temperature during operation. Although these misalignments are expected to produce similar aberrations as those given by the WFC misalignment (thus correctable by repositioning the WFC), linear field astigmatism and curvature can also develop, which will not be compensated by adjusting the WFC alignment state. Also, the internal optical components may develop abnormal variations such as surface deformation due to mechanical/thermal stress. If such problems arise, they can be detected and diagnosed by analyzing the aberration data from the WS measurements in-situ. This will help us plan necessary actions for the problems. Therefore, we wish that the wavefront sensor is capable of sensing at least the so-called *low-order aberrations* and some of the higher-order terms up to Z_{15}, namely wavefront tip/tilt, defocus, astigmatism (Z_5 and Z_6), coma, trefoil (Z_9 and Z_{10}), spherical aberration (Z_{11}), secondary astigmatism Z_{12}, Z_{13}), and quadfoil (Z_{14}, Z_{15}). This requires minimum 7 sub-apertures in each dimension of the WFS.

For monitoring the WFC rigid-body misalignment during observation, it is best to use a stellar object seen by the telescope for the WFS. This means that there must be a sufficient number of stars with certain brightness available in the annular metrology service field for WFS data with sufficiently high signal-to-noise ratio (SNR). In principle, just two stars are sufficient to recover the misalignment errors provided certain constraints on their relative geometry are met; in particular, they cannot be too close to each other or their signals will be essentially degenerate. This is not an

issue for determination of tilts about the x and y axes for which a single star will suffice, but important in sensing the rotation about the optical axis and M1 ROC changes. A sufficient condition to apply is that the two stars be at least 90° apart in the annular metrology service field; that is, they must be separable into opposite quadrants in Figure 1.

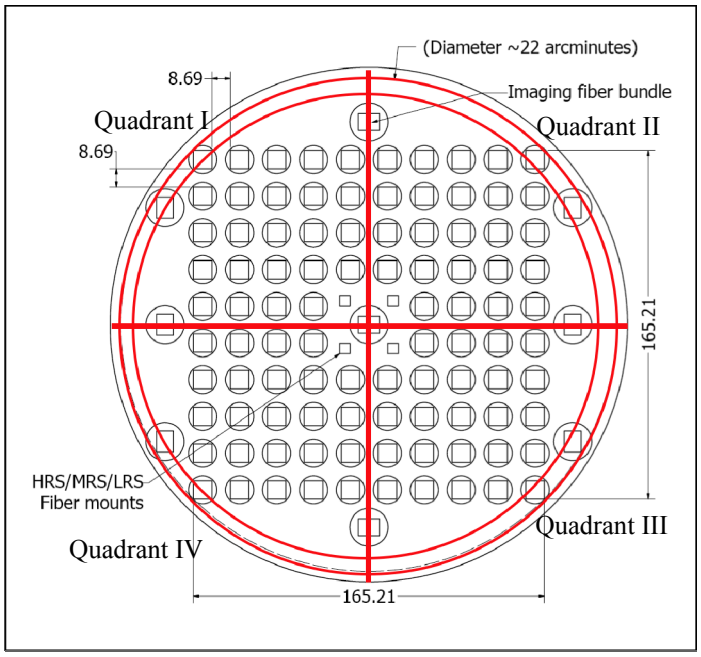

Figure 1 The focal plane of the WFC. The metrology service field is indicated by two red solid circles. The metrology field is divided into four quadrants by the crosshair.

If we state as a requirement that this condition (or better) be met at least 95% of the time, then we can write

$$1 - p_0^4 - 4(1-p_0)p_0^3 - 4(1-p_0)^2 p_0 > 0.95 \quad (1)$$

where p_n is the probability of finding n stars of given minimum brightness within a single quadrant. The second, third, and fourth terms in eq. 1 are the probabilities of finding, respectively, no stars at all, just one, and one or more in adjacent quadrants with exactly zero in the remaining quadrants. They account conservatively for all the configurations that do not satisfy the condition for adequate WFS. The probability of finding a given number of stars down to some limiting magnitude is governed by the Poisson distribution.

$$p_n = \frac{\mu^n e^{-\mu}}{n!} \quad (2)$$

Therefore, we require the mean density of stars for wave-front sensing, $\mu > 2.13$ per quadrant. Each quadrant covers 31.5 square arcmin, so we must have a minimum star density of 243 per square degree. This is very close to the predicted density from the Galaxy model of 254 per square degree for stars of $m_V \leq 16$ at the north Galactic pole[7]. For HET it is therefore conservative to set this as the required limiting magnitude for the wave-front sensing system. Given the expectation that the WFC's misalignment due to change in gravity vector and temperature varies slowly, the update rate of the WFS (thus the integration time) does not have to be fast, but certainly slow enough to sufficiently average out atmospheric aberrations (longer than 30seconds). The spot measurement accuracy can be given by the FWHM of the sub-aperture PSF given by seeing (θ_{seeing}) and SNR as,

$$\sigma_s = 0.425\theta_{seeing} / \sqrt{SNR} \quad (3)$$

where the HET median site seeing of 1.2arcsec is assumed. Eq. 3 is somewhat conservative in a sense that it assumes a read-noise limited case. Although SNR usually appears without the square-root, this version tends to yield optimistic error estimate. Also, there is error contribution from pixelation effect[22]. Thus, we adopt Eq. 3 for our analysis as an upper limit. Assuming K5 spectral type, which represents the commonest type of stars in the sky in the range of magnitudes likely to be used for the WFS, the estimated photons, SNR, and spot measurement accuracy per sub-aperture at the WS detector for two different V magnitudes are shown in table below.

Table 2. Photons, SNR, spot centroid accuracy per sub-aperture
(plate scale=0.25arcsec/pix, 18x18 pixels per sub-aperture, $m_{v,sky}$=20, and 5e- read noise assumed).

m_V	V-band Photon flux[8-12] [photons/m^2/s]	Telescope throughput	Sub-aperture density	Photons, SNR, spot measurement accuracy per sub-aperture					
				Δt=30 sec			Δt=60 sec		
				Photons	SNR	σ_s [as]	Photons	SNR	σ_s [as]
16	3500	0.18	7 x 7	38583	188	0.037	77166	272	0.031
			16 x 16	7385	70	0.061	14770	110	0.048
17	1394		7 x 7	15360	112	0.048	30720	165	0.039
			16 x 16	2940	36	0.085	5880	61	0.064
18	555		7 x 7	6115	62	0.065	12230	97	0.052
			16 x 16	1170	17	0.123	2341	30	0.093

These parameters are to be used in computing the uncertainty in the WFC misalignment estimation.

2.2 Models.

Although the telescope optical design is given by the Zemax[13] optical prescription, we modeled the telescope and beam propagation through the telescope in a separate analysis environment, using Optical Programming Library (OPL)[14], primarily to ease the transition between the ray-tracing-based wavefront propagation through the telescope model and the Fast-Fourier-Transform-based (FFT) beam propagation through the wavefront sensor model, and secondarily to parallelize computationally intensive part of the code (e.g. in ray-tracing and FFT-beam propagation routines) for speeding up Monte-Carlo simulations. This separate environment is written in C-language and we used the OPENMP[15] library for the code parallelization. The primary mirror is modeled as a collection of 91 hexagonal surfaces located at their nominal positions. These segments can be translated along and rotated about predefined local x,y,z axes. Surface deformation of individual segments is described by means of the standard Zernike polynomials. Misalignment and surface deformation of other optical elements such as the mirrors in the WFC are described in the same fashion. The tracking is modeled by rotating the primary mirror segments about the center of curvature of M1, with respect to the WFC optical components.

For ray tracing, a 10m diameter collimated beam from a point source at a certain field position is modeled as a grid of rays within the beam aperture pointing toward the telescope entrance pupil that is at the center of curvature of the telescope M1. The size of the ray grid is determined by the pixel scale, desired number of pixels per sub-aperture, and the quantum efficiency (QE) averaged wavelength of the WS detector, which are user-input parameters. The ray-grid size is usually much larger than the desired size of detector pixel grid. Thus, at the end of the FFT beam propagation (to be discussed shortly), the ray-grid is binned into the detector grid. The bin size is given by the pixel scale and the QE-averaged wavelength. Before tracing the stellar rays, a few pilot rays are first traced through the telescope model to compute all first order parameters and to identify conjugate planes (including the exit pupil) of the telescope. The stellar rays are then traced in a sequential fashion through the individual optical components in the telescope model via Snell's law. The ray-tracing stops when all rays arrive at the focal surface of the WFC. Subsequently, a reference Gaussian sphere is created at the vertex of the exit pupil of the WFC centered at the location of the central ray. The stellar rays are then traced back to the Gaussian sphere. The optical path lengths of the stellar rays are then subtracted from that of the principal (i.e. central) ray, resulting in the geometric optical path difference map (i.e. wavefront).

The computed wavefront is divided into sections according to the geometry of the sub-aperture grid. Each section is then Fourier-transformed via FFT to produce the sub-aperture PSF over the detector plane. During the FFT, the PSF is embedded into a large grid to prevent aliasing effect. Each PSF is then normalized to the appropriate sub-aperture photon energy given by the stellar magnitude, temperature, and sub-aperture grid size, which are also user-input parameters. Adding and binning all sub-aperture PSFs to the final detector grid then produce the Shack-Hartmann spot image given by the wavefront. Next, the centroid of each SH PSF is computed. The code provides two centroid algorithms. Both algorithms first find the peak of the sub-aperture PSF and use it as the initial guess of the subsequent centroid refinement. Only those pixels with energy level above a predefined threshold (50% of the peak value) are fed to the centroid algorithms. The first centroid algorithm computes a more refined centroid by directly averaging the x and y pixel positions weighted by pixel values, while the second algorithm runs the *Newton-Raphson* optimization to search for the centroid that gives the optimal fit of a Gaussian or Moffat function to the given SH PSF. The reference centroids are then subtracted from the measured PSF centroids to yield the final wavefront slope measurements. Here, we assume that the reference centroid positions of individual sub-aperture are obtained by propagating a flat wavefront through the WS model. Two examples of simulated SH WS images are shown in Figure 2.

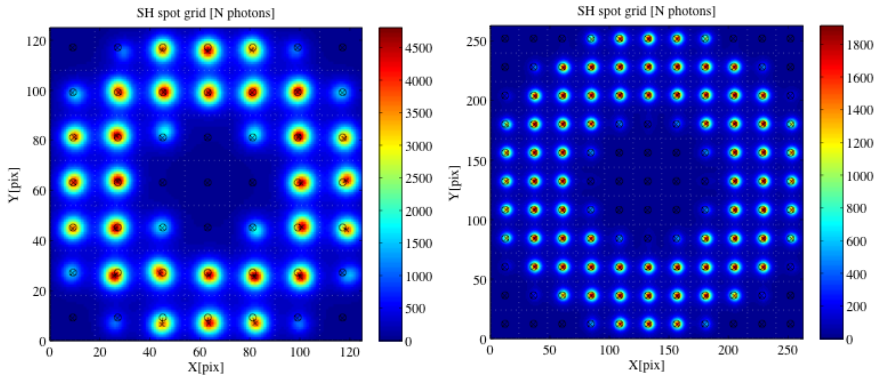

Figure 2 Example SH WS images: 7x7 (left) and 11x11 (right) sub-aperture.

For the wavefront reconstruction, we use the modal sensing approach. The wavefront slope data ($\vec{w}$, 2N×1 vector) is related to the WFC misalignment vector ($\delta\vec{u}$, 6×1 vector) by Eq. 4.

$$\vec{w} = \mathbf{A}\,\vec{z} = \mathbf{A}\,(\mathbf{R}\,\delta\vec{u} + \vec{z}_0) \quad \Rightarrow \quad \delta\vec{w} = \vec{w} - \mathbf{A}\,\vec{z}_0 = \mathbf{A}\,\mathbf{R}\,\delta\vec{u} \tag{4}$$

Here $\vec{z}_0$ is the known aberration coefficient vector (e.g. field aberrations). **R** is a M×7 alignment sensitivity matrix. Multiplying it to $\delta\vec{u}$ yields the alignment-driven aberration vector ($\delta\vec{z}$). **A** is the 2N×M Zernike slope matrix that relates the aberration coefficients to the sub-aperture slopes. Note that N is the number of sub-apertures used in the analysis. M is the number of Zernike modes for reconstruction. Also note that $A_{i,j}$ and $A_{i+N,j}$ are the x and y slopes of the *j*-th Zernike polynomial, respectively, within the *i*-th sub-aperture and can be obtained by fitting a plane to the polynomial in the sub-aperture. $\delta\vec{w}$ represents the alignment-driven slope aberration. By solving Eq. (4) and multiplying -1 to the solution vector, one can obviously obtain the WFC alignment correction estimate ($\Delta\vec{u}_a$).

$$\Delta\vec{u}_a = -\mathbf{R}^*\left(\mathbf{A}^*\delta\vec{w}\right) \tag{5}$$

where * means pseudo-inverse. Here, the alignment sensitivities of the Zernike coefficients are given as follows.

$$\begin{aligned}
Z_2 &= 2.19x_d - \left(z_r / 2.257\right)(r/11)\sin\theta + 7.03\Delta_{GRoC}(r/11)\cos\theta + 1.597y_t \\
Z_3 &= 2.19y_d + (z_r / 2.257)(r/11)\cos\theta + 7.03\Delta_{GRoC}(r/11)\sin\theta - 1.597x_t \\
Z_4 &= -z_d / 4.111 + 120\Delta_{GRoC} \\
Z_7 &= -x_t / 1.763 \\
Z_8 &= y_t / 1.763
\end{aligned} \tag{6}$$

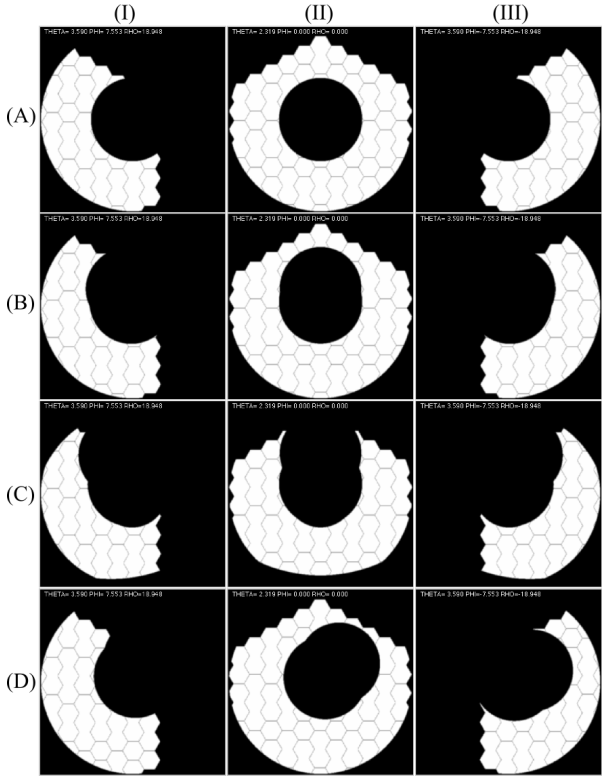

Figure 3 HET pupil seen at four field locations (from top to bottom) and three tracker positions along a particular trajectory (from left to right).

where (*r, θ*) is the field position of the wavefront sensor star in the polar form. A special attention needs to be given to the GRoC control. The GRoC has essentially the same effect as the WFC defocus does: blurring stellar images and adding defocus aberration to WFS signals. As a result, it is difficult to distinguish these two parameters just by analyzing the WFS aberration data. Our plan for updating the GRoC is as follows. We use a distance measuring interferometer (DMI) to maintain the physical separation between the WFC and the M1 as the GRoC drifts[3]. This will accumulate defocus aberration to the WFS signal, thereby increasing the required amount of the WFC focus correction given by the WFS. Once the amount of the *accumulated* WFS-based focus correction reaches a certain upper limit (which must be set by the required seeing convolved image quality specification), the accumulated value is applied as an offset to the GRoC value. At the same time, the DMI zero point also needs to be offset by this value.

In Eq. 5, one needs to take into account two effects: i) cross-coupling among aberrations and ii) higher-order aberrations aliasing into sensed low-order aberration modes[16]. The main result from these effects is that $\Delta\vec{u}_a$ change whenever the number of reconstructed terms changes (i.e. sub-optimal coefficients). Both effects appear when **A** in Eq. (4) is non-orthogonal. Although **A** is based on Zernike polynomials that are certainly orthogonal (but only over a circular pupil), it is essentially given by the mean values of the first derivatives of Zernike polynomials, which are not orthogonal (even over the unit disk). To minimize these

effects, it is often done in practice to reconstruct only the first few aberrations when wavefront can be very well described by those aberrations. When this is not the case due to variations in unknown field-dependent aberrations, surface figure errors, vibration, local seeing effects, etc., one may reconstruct as many aberration modes as possible. These approaches do not provide a complete solution to the problem in general although, in some cases, we found that limiting the number of reconstructed modes to low-order terms (that are mainly affected by the WFC misalignment, up to Z_{11}) can help to minimize this effect. For the wavefront reconstruction, the effect on the WFS slopes of high-order aberrations that are known from the telescope aberration model (e.g. higher-order field aberrations in particular) are explicitly measured and recorded. For any given field position of a WFS star, these known terms can be subtracted from the WFS slope data before the reconstruction step. However, simply fitting Zernike polynomials to the WFS slope data in the reconstruction step is shown to be unstable, especially when the pupil shape significantly deviates from the unit disk. In Figure 3, the HET pupil shape is shown at four field positions (from top to bottom row) and three tracker positions in a particular trajectory (from left to right column). Instead, orthonormal slope polynomials are fitted to the slope data to obtain the orthonormal slope aberration coefficients. This is shown to be effective (Sec 3.4).

Nonetheless, for the HET WFS, this issue is particularly important not only because of dynamic pupil shape variation, but because of several possible factors that can introduce unknown and unsensed higher-order aberrations (e.g. local dome seeing issue and poorly aligned and figured primary mirror segments). Therefore, using a set of orthogonal slope polynomials for each WFS measurement can be useful toward the edges of trajectories in particular. It turned out that constructing orthonormal slope polynomials and applying them to the slope measurements on the fly can be quite feasible and effective: all we need to do is to compute the conversion matrix **C** between the Zernike slope matrix **A** and the desired orthonormal slope matrix **V** over a given pupil and sensor geometry ($\mathbf{A} = \mathbf{V}\,\mathbf{C}^{\mathrm{T}}$). It has been found that **C** is given by $\mathbf{F} = \mathbf{A}^{\mathrm{T}}\mathbf{A}/\mathrm{N}$ in the following way [17-18]:

$$C_{ii} = \sqrt{F_{ii} - \sum_{k=1}^{i-1} C_{ik}^2}\,, \quad C_{ij} = \frac{F_{ij}}{C_{jj}} - \sum_{k=1}^{j-1} \frac{C_{ik} C_{jk}}{C_{jj}} \tag{6}$$

where F_{ij} is the (i,j) element of **F**.

Given the relation between **A** and **V**, it is easy to show the following.

$$\delta\vec{w} = \mathbf{A}\,\delta\vec{z} = \mathbf{V}\left(\mathbf{C}^T \delta\vec{z}\right) = \mathbf{V}\,\delta\vec{s} \tag{7}$$

Clearly, the orthonormal slope aberration coefficients ($\delta\vec{s}$) is related to the Zernike aberration coefficient via **C**. Using these relations, we obtain the following.

$$\Delta\vec{u}_v = -\left(\mathbf{C}\,\mathbf{R}\right)^* \delta\vec{s} = -\left(\mathbf{C}\,\mathbf{R}\right)^* \mathbf{C}^T \delta\vec{z} \tag{8}$$

The term in the first round bracket corresponds to the optimal alignment sensitivity matrix over the given geometry. The term in the other bracket is essentially the slope aberration coefficient estimate. This estimate has to be unique as **V** is orthonormal. As a result, the alignment correction $\Delta\vec{u}_v$ has to be unique. Eq. 7 shows that the usual Zernike aberration coefficient estimate ($\delta\vec{z}$) can be used to obtain the unique alignment correction estimate by means of **C**. In fact, $\delta\vec{z}$ and **C** are all natural by-product of the usual least-square Zernike fit, meaning that the estimation can be done in the usual way, but with one additional procedure of computing **C** based on **R** using Eq. 6, which can be done straightforwardly.

2.3 Noise propagation.

Noise in the slope measurements from the Shack-Hartmann wavefront sensors will propagate into the reconstructed aberration modes. Uncertainties will arise primarily from photon noise, sensor read noise, and aliasing effects that can not be removed by the anti-aliasing procedure. To a reasonable approximation, and to get a straightforward estimate of the errors, we can take the noise in all illuminated sub-apertures of the Shack-Hartmann WFS to be the same and independent. Slope aberration modes are recovered from Shack-Hartmann slope measurements by multiplying a reconstruction matrix **B** to a vector of the spot positions ($\delta\vec{w}$). With σ_n^2 as the noise variance in a single sub-aperture, the modal error propagators are given by the leading diagonal elements of the matrix $\sigma_n^2 \boldsymbol{B}\boldsymbol{B}^T$.

The requirement on noise should be set by the worst case, illustrated in the figure below. Assuming a 7x7 sub-aperture density, total 12 sub-apertures are illuminated. The worst error propagators in this case are 16880, for the two tilt modes. Thus a 1″ rms uncertainty in the spot positions will yield an uncertainty of √16880 = 130 rad rms in the estimate of Z_3, and an uncertainty 130/2.19 = 59.3 μm in x_d. To ensure a measurement that will discriminate between an aligned versus a misaligned system with >99% confidence, we set the absolute limit on the rms uncertainty in x_d at 0.3 times the

alignment tolerance, or 3 μm. This leads to a requirement on the standard deviation in the spot position measurements of 3/59.3×1″ = 0.05″. This corresponds to SNR ~ 104. As shown previously, stars of 16th magnitude are likely to be available for sensing alignment errors with >95% probability. Conversely, the required SNR of 104 implies, based on the SNR estimates given in Table 1, that a 7x7 WFS could run as fast as twice a minute even with a m_V=18 star if necessary. The density of stars to this magnitude is ~1000 per square degree at the north Galactic pole, thus more stars will be available for the WFS.

3. ANALYSIS

3.1 WFS sensitivities to M1 errors.

Using our simulation code, we first conducted a sensitivity analysis to quantify the effect of M1 errors. The perturbation parameters are varied one at a time according to a Gaussian or Uniform probability distribution. For each parameter, we constructed 201 random realizations. We then computed the resultant distributions of errors in the alignment estimation (i.e. difference between the estimates and true values of the WFC alignment parameters). In the plots below, we denote the difference in each alignment parameter by δx, δy, δz for decenters/defocus, δRx, δRy, δRz for tip/tilt/rho, respectively. In the analysis, we also randomly perturbed the WFC alignment parameters within the ranges given below.

Table 3. **The ranges of WFC rigid-body misalignment (Uniform distribution)**

Decenter (x_d,y_d)	Defocus (z_d)	Tip/tilt/rho (x_t,y_t,z_r)
±20 μm (spec: ±10 μm)	±20 μm (spec: ±10 μm)	±15 arcsec (spec: ±4 arcsec)

For this study, we assumed two m_V=18 WFS stars at (0,+11) and (0,-11) arcmin fields. A 7x7 sub-aperture grid was used. The sub-aperture field was set to 4.5x4.5arcsec^2 to comfortably accommodate the seeing PSF with a plate scale of 0.25arcsec per pixel. We assumed 60sec exposure time with 1.2arcsec seeing. The tracker is assumed to be at the center of the track. The GRoC error is not considered in this analysis. The list of perturbation parameters is given in Table 4.

Table 4. Perturbation parameters for the sensitivity analysis.

Parameter	Distribution	Case I	Case II	Case III
Segment tip/tilt	Gaussian	±0.1 arcsec (rms)	±0.2 arcsec (rms)	±0.5 arcsec (rms)
Segment piston	Gaussian	±10 μm (rms)	±50 μm (rms)	±100 μm (rms)
Segment astigmatism	Gaussian	--	±0.36 wv (rms)	±0.91 wv (rms)
Segment radii of curvature	Uniform	--	±1 mm (p-p)	±2 mm (p-p)

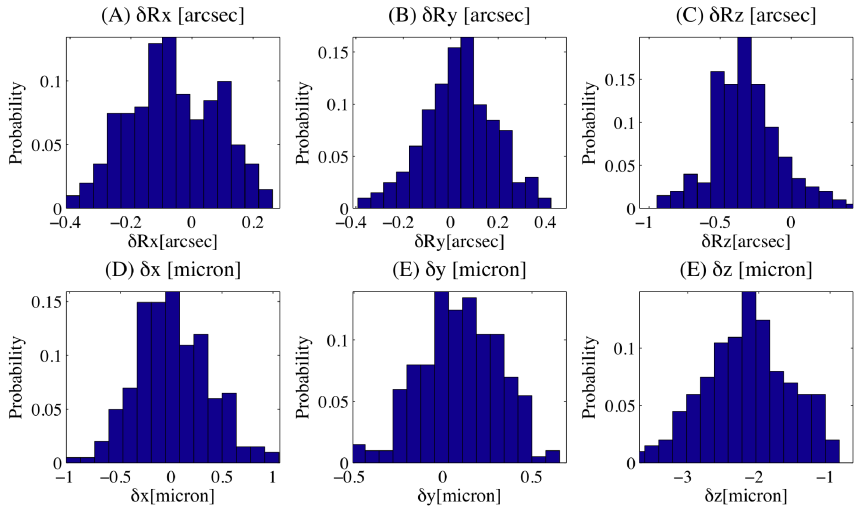

Figure 4 Distributions of alignment estimation errors in the nominal case (Everything is nominal except the WFC alignment. See Table 3).

We first present the nominal case result where everything is perfect except the WFC alignment is perturbed within the ranges in Table 3 (Figure 4). The estimation errors of decenter and tip/tilt are distributed around zero whereas the mean values of the rho and defocus errors (-0.3as and -2.1 μm, respectively) are slightly shifted. The distribution widths at 99% level are ±1.26 μm, ±0.78 μm, ±2.08 μm for x, y decenters and defocus and ±0.51 as, ±0.54 as, ±0.85 as for tip, tilt, and rho. For this particular case, the noise propagator is 1136, meaning 34 rad rms for 1arcsec rms uncertainty in the spot position measurement. The SNR in this case is 131 and σ_s ~0.043 arcsec. Using Eq. 3, the upper limit on the estimation error of x_d is ~ 2.0 μm at 99% level.

The error from the simulations is clearly better than this, but using SNR instead of √SNR in Eq. 3 gives an error estimate of 0.18 μm at 99% level that is roughly 7 times overly optimistic. The following table shows the WFS sensitivities to M1 errors.

Table 5. Sensitivities to M1 segment errors (99.9% level).

Parameter		δx[μm]	δy[μm]	δz[μm]	δRx[arcsec]	δRy[arcsec]	δRz[arcsec]
Segment tip/tilt (rms)	0.1 arcsec	±5.03	±5.42	±10.8	±3.77	±3.11	±10.2
	0.2 arcsec	±11.4	±10.9	±21.4	±7.27	±6.42	±20.1
	0.5 arcsec	±37.6	±37.1	±55.9	±26.6	±21.1	±64.7
Segment piston (rms)	10 μm	±0.21	±0.34	±0.49	±0.66	±0.62	±1.09
	50 μm	±5.63	±4.79	±19.4	±6.84	±4.60	±7.27
	100 μm	±9.23	±11.12	±53.1	±13.9	±9.7	±23.1
Segment astigmatism (rms)	0.36 wv	±3.69	±3.18	±6.87	±2.64	±2.65	±5.98
	0.91 wv	±10.55	±8.97	±18.1	±6.87	±7.54	±16.5
Segment RoC (p-p)	1.0 mm	±5.9	±4.93	±10.8	±4.27	±4.15	±8.96
	2.0 mm	±15.6	±6.13	±19.4	±5.43	±7.33	±17.2

Based on these sensitivities, we derived the required tolerances on the segment errors. Assuming that these errors are added in quadrature, we allocated appropriate weights to each error. As δz is more sensitive than other parameters, we determined the required limit for the segment errors such that δz becomes within ±10 μm. The resultant limits on the M1 segment errors are: ±0.06 arcsec in tip/tilt, ±30 μm in piston, ±0.28 wv in surface astigmatism, and ±300 μm in RoC. Some of these are smaller than the currently estimates for these errors.

Table 6. Currently estimated values for the M1 segment errors and expected estimation errors.

Segment errors	Tip/tilt[arcsec]		Piston[μm]		Astg.[wv]	RoC[mm]	
Estimated values	±0.48 (p-p)		±75 (p-p)		±0.20 (p-p)[19]	±0.7 (p-p)	
Estimation error	δx[μm]	δy[μm]		δz[μm]	δRx[arcsec]	δRy[arcsec]	δRz[arcsec]
Expected values (p-p)	±33	±33		±63.4	±14	±14	±35

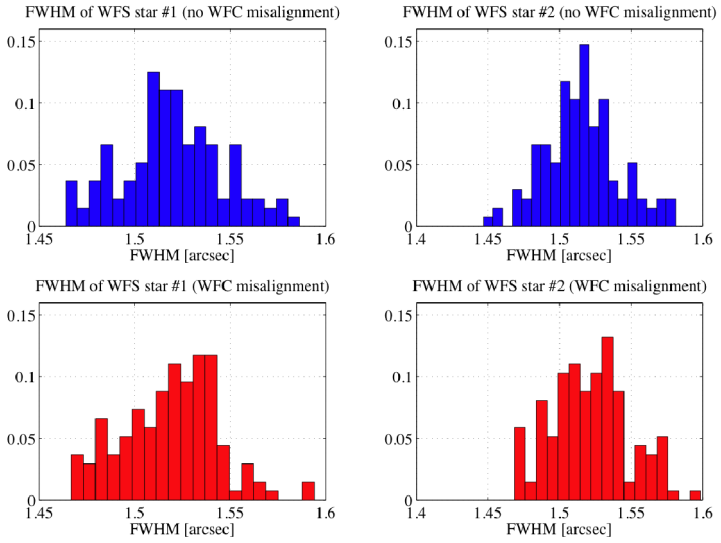

Figure 5 Distributions of the seeing convolved FWHM of two WFS stars before (blue) and after (red) WFC alignment corrections in the presence of M1 segment errors (1.2arcsec seeing was used).

The known segment error values were then multiplied by the alignment sensitivities given by Table 5 to produce the expected WFS alignment estimation errors (Table 6). The expected estimation errors are roughly a factor 3 larger than the required WFC alignment tolerances to ensure δz within ±10 μm. However, the larger WFC alignment estimation error does not necessarily mean that the image quality of the telescope is worse than what the telescope can deliver with these M1 errors. As we can see below, the telescope image quality is very much governed by the magnitude of the M1 segment errors. Beyond a certain level, the image quality degradation due to WFC misalignment is buried within that given by the M1 segment errors, thereby even a perfect WFC alignment correction does not improve the telescope image quality. Figure 5 illustrates this.

Here the distributions of the FWHM of two WFS star are plotted. The top row shows the FWHM of two stars (left and right column) when only M1 segment errors were given without WFC misalignment. When we also included WFC misalignment and made corrections to it, the stellar FWHM distributions look like the histograms in the bottom row. It is clear that the distributions in the top and bottom rows are not significantly different. The floor of the

telescope image quality is essentially set by the M1 segment errors so that any further adjustment of the WFC alignment does not improve the situation significantly. After all, the WFS is not meant for fixing the M1 segment errors.

3.2 WFC internal misalignment.

Although the optical components internal to the WFC are to be secured to their mounting structures, there will be small amounts of alignment variations of the components, the four mirrors in particular, during operation due to the change in gravity vector and temperature. From the Finite Element Analysis (FEA) of the WFC structure model, the expected operational alignment variations in the alignment of the internal components can be computed. These errors are likely to be repeatable and thus can be measured and built into the telescope mount models. However, to test the WFS performance in the face of these errors, we perturbed the internal elements within somewhat extreme ranges of these variations (Table 7) in the WFS simulation. Note that the M1 segment errors were not included here, but the WFC alignment parameters were perturbed within the ranges in Table 3.

Table 7. Expected ranges of the operational alignment variation of the WFC internal optical components

Components	x[μm]	y[μm]	z[μm]	Rx[arcsec]	Ry[arcsec]
M2	±50	±50	±50	±2	±2
M3	±50	±50	±50	±2	±2
M4	±20	±20	±10	±1	±1
M5	±20	±20	±10	±1	±1
FOCAL PLANE	±50	±50	±30	±2	±2

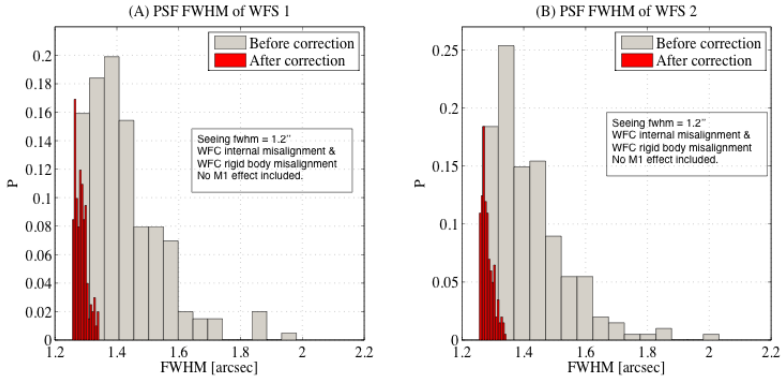

Figure 6 Distributions of the seeing convolved FWHM of two WFS stars before and after WFC alignment corrections in the face of WFC internal misalignment.

As the internal optical elements are misaligned, it is more instructive to see how well the telescope image quality is recovered rather than checking the WFC alignment estimation errors. Figure 6 shows this. Before the corrections, the distributions of the seeing convolved FWHM of two WFS stars were broadly spread between 1.3arcsec and 2arcsec. The distributions were then collapsed toward the seeing convolved nominal telescope image quality of 1.3arcsec. Note that, in these 201 random realizations, the WFC was also randomly perturbed within the ranges specified in Table 3. This clearly demonstrates that the WFS will be able to catch the WFC internal misalignment effects so that the alignment corrections compensate for these and those from the WFC rigid-body misalignment. This compensation was evenly applied across the field of the telescope. Although the telescope image quality can be recovered, there will be some kind of control feedback discrepancy between the DMI/TTS and the WFS. It will be necessary to coordinate the role and priority in sensor feedback to avoid such discrepancy [3].

3.3 Effect of pupil drift during exposures.

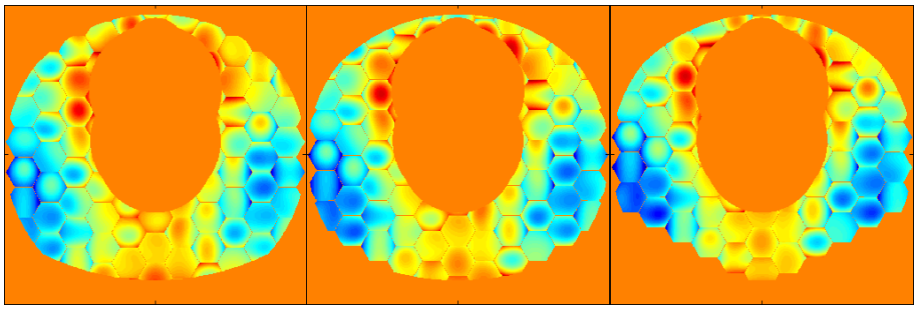

Figure 7 Telescope wavefront map at the beginning (left), middle (center), and end (right) of a 60 sec exposure as seen by a wavefront sensor at (0,+11 arcmin) field.

Due to the tracking nature of the telescope, it is inevitable that the telescope pupil will drift along the direction of a track during a finite WFS exposure time. This is illustrated in Figure 7 where the telescope pupil at the beginning, middle, and end of a 60sec. exposure. A potential issue with this effect is that the

wavefront sensors will scan across different sections of the M1 with different segment errors.
To investigate this effect, we modeled this by a series of *N* wavefront maps. The time different between two maps was given by $\Delta t=t_{exp}/N$ where t_{exp} is the total exposure time. The tracker was simulated to move at some rate during Δt. The required number of wavefront samples (N) depends on how accurately one wants to model this effect and how quickly the pupil geometry sweeps over the primary. The WFC pupil moves across the primary mirror at about 2 mm per second. For 60 sec exposure, the pupil travels 120 mm during the integration over the primary mirror, which is about 10% of the size of a mirror segment (~1.154 m apex-to-apex). It is less likely though that the primary mirror segments show large variations in their characteristics during this short period of time. The actual travel of the tracker itself is to be about half of the pupil travel (~60 mm per min). Therefore, it is also unlikely that the tracker and WFC exhibit large amounts of gravity-induced variations. Given these assumptions, we choose N=10 in simulating this effect.
We applied this model to a set of 201 random realizations where the WFC alignment was perturbed according to Table 2 and the M1 segment were tilted by 0.1 arcsec in rms. Table 8 below shows the errors in estimating the WFC rigid-body misalignments using the measurements from two WFS in the face of the pupil drift effect. For a comparison, we also list the errors in the case without the pupil drift effect (i.e. snapshot assumption). These values have been shown in Table 5 for the 0.1 arcsec segment tip/tilt case. The estimation errors with the pupil drift effect are effectively same as the values without the effect, illustrating a minimal impact of the pupil drift to the WFS.

Table 8 WFC alignment estimation errors in the presence of 0.1arcsec M1 segment tip/tilt error (with and without the pupil drift effect).

CASE	δx[μm]	δy[μm]	δz[μm]	δRx[arcsec]	δRy[arcsec]	δRz[arcsec]
Without pupi drift	±5.03	±5.42	±10.8	±3.77	±3.11	±10.2
With pupil drift	±4.91	±4.91	±9.63	±3.61	±3.61	±10.5

3.4 Random perturbation analysis along a track.
In the previous analyses, the WFC was assumed to be at the center of a track (i.e. WFC's 10 m circular pupil is centered at the vertex of the M1). Therefore, the overall pupil shape was close to the unit disk. During a track, however, the pupil of the WFC will sweep across the M1 and the pupil shape can significantly deviate from the unit disk around the edges of the track. In such situation, the Zernike-based modal sensing can be affected by aberration couplings and higher-order aliasing effects. Here, we randomly perturbed the WFC alignment while the telescope pupil changed according to one particular tracker trajectory. The trajectory consists of 166 trajectory points. At each trajectory point, the pupil shape is different. Some of the snapshots of the telescope pupil along this trajectory are shown in Figure 8. At each point, we randomly perturbed the WFC alignment. The aberration coefficients were then obtained by fitting Zernike polynomials and orthonormal slope polynomials. Based on these aberration coefficients, we estimated the WFC misalignment. We assumed that only one wavefront sensor was available.

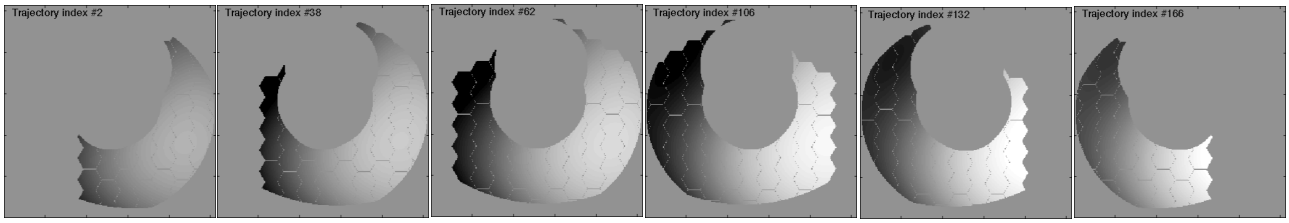

Figure 8 HET pupils seen at the center of the field along one example trajectory. A sample optical path difference is mapped onto the pupils with a grey scale.

Firstly, we used first 7 polynomials in the fitting process and the resultant errors in WFC misalignment estimates are plotted as a function of the trajectory index in Figure 9. Blue curves are from using 7 Zernike polynomials while red curves are from using 7 orthonormal slope polynomials. Note that we applied a zero mean Gaussian random fluctuation to the wavefront with RMS error that is equivalent to atmospheric turbulence of $D/r_0=1$. No M1 errors were included. The estimates based on Zernike polynomials clearly show variations in the error curves, which are obviously not intrinsic to the zero mean random errors used in the simulation. In contrast, the estimates based on the orthonormal slope polynomials exhibit nearly flat error curves with randomly fluctuating features around them.

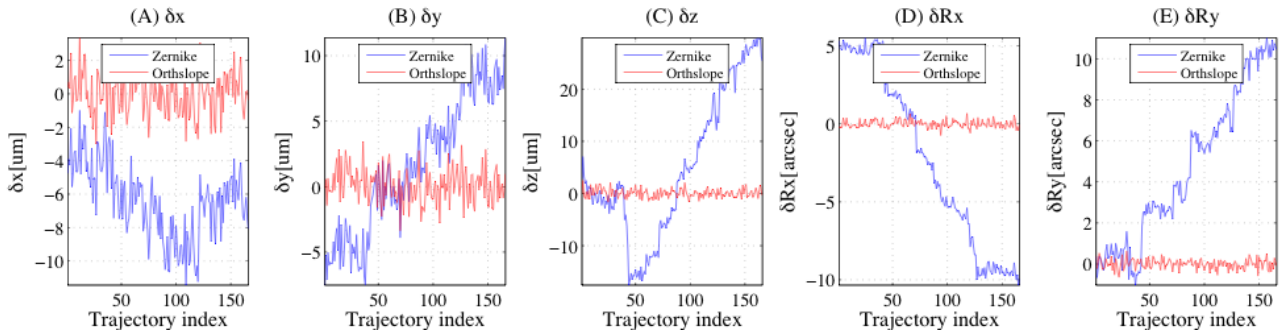

Figure 9 WFC misalignment estimate along the example trajectory based on the aberration coefficient estimates from fitting 7 Zernike (Red curves) and orthonormal slope polynomials (Blue curves) to wavefront.

Applying the same perturbations to the WFC, we performed the same misalignment estimation, but based on the aberration estimates by fitting the first *14* Zernike and orthonormal slope polynomials. The estimates given by the Zernike polynomials (blue curves) again show variations that are not intrinsic to the applied perturbations. In this case, however, the magnitudes of the variations are much smaller than in the previous case. The non-intrinsic variations that were in the tip/tilt estimation error curves of the previous case are gone in this case. The estimation error curves based on the orthonormal slope polynomials remain the same as in the previous case. Notice the different y-axis scale in Figure 10 from those in Figure 9.

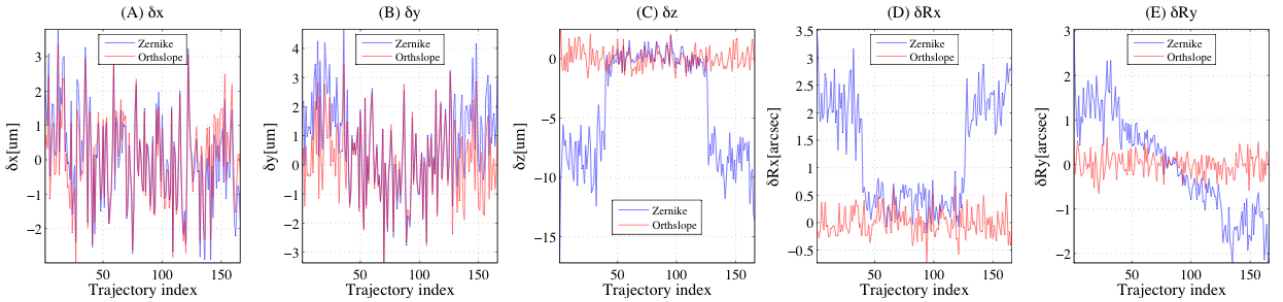

Figure 10 WFC misalignment estimate along the example trajectory based on the aberration coefficient estimates from fitting 14 Zernike (Red curves) and orthonormal slope polynomials (Blue curves) to wavefront.

The wavefront sensors are to be used not only for WFC alignment, but also characterizing the (wavefront or slope) aberrations of the telescope in-situ. Thus, it is important to see how effective the use of orthonormal polynomials in the WFS would be. Figure 11 shows this. In this case, we used the same WFS parameters except denser sub-aperture geometry (16x16). This higher-order wavefront sensor should be able to comfortably estimate up to 36 aberration coefficients. We modeled the telescope wavefront seen at the (0,+11) arcmin field with random wavefront error equivalent to D/r_0=1.0. We estimated the first 14 aberration coefficients using the Zernike polynomials and orthonormal slope polynomials. The same trajectory as in Figure 6 was used. Each plot in Figure 11 shows the relative error in each aberration coefficient estimate against the trajectory index. The result clearly shows that the aberration coefficients given by the Zernike polynomials significantly deviate from the true coefficient values, whereas those given by the orthonormal slope polynomials are very close to the true slope coefficient values.

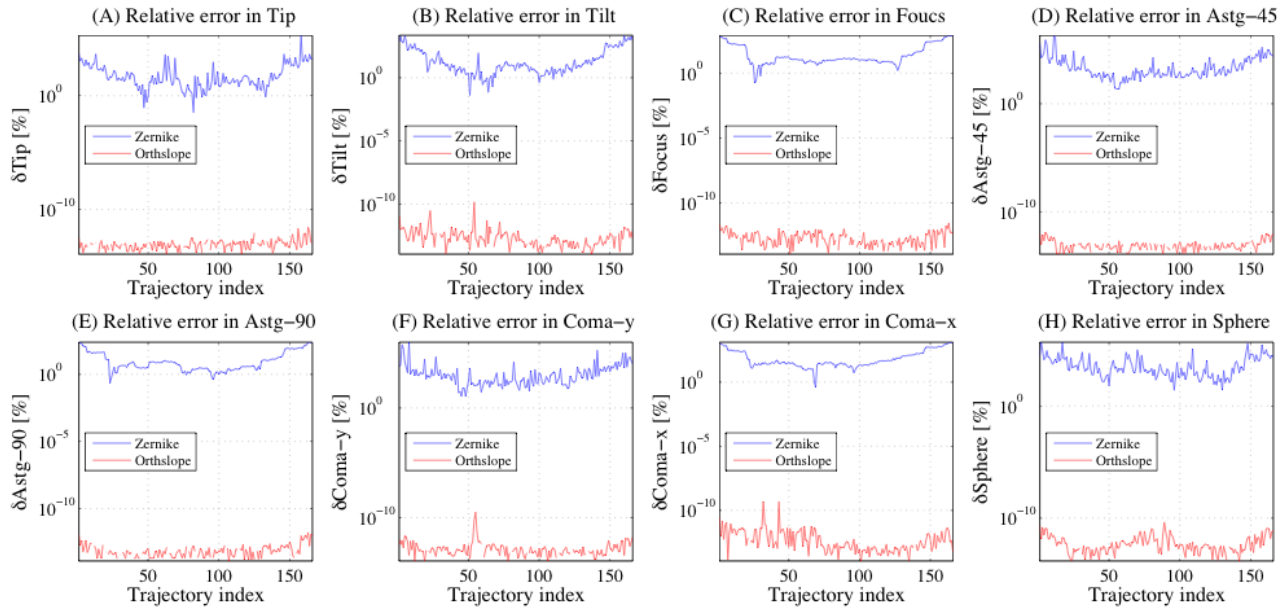

Figure 11 Relative errors in the aberration coefficient estimates given by the Zernike polynomials (blue curves) and orthonormal slope polynomials (red curves) along the trajectory as in Figure 8.

4. WFS PRODUCTION & TEST PLAN

Commercially available wavefront sensors could do most of the basic functions of the WFS. However, for our application, it turned out that most of the off-the-shelf wavefront sensors we located were less ideal in terms of physical size, sub-aperture density, etc. For the WFC, we therefore plan to build three wavefront sensors. Two of these will be low-order (7 x 7 sub-aperture) Shack-Hartmann wavefront sensors operating within the metrology service field. These are to be used during science observations to produce feedbacks for the WFC alignment control as well as to monitor the optical characteristics (WFC internal alignment, mirror surface deformation, etc.) of the telescope in-situ. Each sub-aperture is approximately 4.5x4.5 arcsec^2 with a plate scale of 0.25 arcsec per pixel. Given the telescope throughput, the low-order wavefront sensors are expected to reach SNR ~ 110 in a 60sec exposure for a m_v=18 star in the V filter, giving sufficient accuracy for the WFC alignment estimation. In addition to the low-order sensors, there will be another wavefront sensor that uses a denser sub-aperture (16 x 16). This higher-order wavefront sensor is to operate at the center field of the telescope and to be used during the initial commissioning of the telescope upgrade to help various optical tests of the WFC, the new tracker, and on-sky tests. This higher-order wavefront sensor is to also serve as the fiducial wavefront sensor against which the other two low-order sensors are to be calibrated.

The design of these wavefront sensors is as follows: A collimation lens (off-the-shelf achromatic doublet) takes the telescope focus and forms the telescope pupil onto a lenslet array. The collimation lens design is to be chosen so as to produce as flat wavefront as possible from a point source. This prevents the reference spots from being too much offset within each sub-aperture and thus preserves the dynamic range set by the sensor geometry as much as possible. The lenslet array produces a Shack-Hartmann spot image on the input surface of a coherent imaging fiber bundle from Schott[20]. The fiber bundle consists of several hundred thousand single mode 10 micron-core fibers packed in a rectangular format. By use of the fiber bundle, we can leave the small sensor head within the crowed focal plane region while letting the bulky CCD and associated electronics remotely located in a separate electronics box. The SH spot image is then transmitted through the approximately 4m-long fiber bundle to the output surface and then reimaged by an imaging lens onto the CCD. We plan to use a FLI Microline CCD for the imaging sensor. The collimation lens is to be separately tested by using an interferometer and its field aberrations are to be characterized. The imaging lens in between the fiber bundle output and the CCD can be off-the-shelf achromatic doublet. A filter can be located in this output end optical train for an appropriate spectral filtering. The alignment between the fiber bundle output, the imaging lens, and the CCD can be done by adjusting the lens until making a well-focused image, with a correct magnification, of a well structured target object (fed into the fiber bundle) on the CCD.

In order to achieve maximum stability possible during operation, we plan to glue the lenslet array to a precision-machined glass block and to glue this block to the input surface of the fiber bundle. The glass block is to accommodate the required separation between them due to focal length of the lenslet array. All elements in this lenslet unit are shaped in square. The collimation lens can also be shaped in square. Thus all elements can be glued to into a square-shaped tube structure with precision machined mounting features for individual elements. We expect that this approach can make the sensor stable through the expected temperature variation.

Once the integration is complete, we plan to set a lab calibration test for the sensor to identify the SH reference spot image. A small pinhole illuminated by a light source from the back can be placed at the focus of the collimation lens. The pinhole produces a spherical wavefront and the collimator feeds the nominal wavefront due to the collimator itself. The SH spot image formed by the lenslet array becomes the reference image for subsequent wavefront sensing. Though the sensor is likely to be structurally rigid and thus we expect to perform this calibration rarely, it would be useful to do the same calibration through the expected temperature swing to see the variation in the reference spot image. An initial tolerance analysis of the wavefront sensor indicates relaxed optical tolerances on the optical elements, but more detail analysis is in progress.

5. SUMMARY

In this paper, we described the analysis of the wavefront sensing for active alignment of the HET WFC. Two major challenges to the WFS are the M1 segment errors and the dynamic telescope pupil shape variation. The analysis indicates that the WFS should produce accurate correction estimates for the WFC alignment. In the presence of the M1 segment errors, the estimation accuracy becomes degraded. At the same time, however, the telescope image quality also degrades, which cannot be recovered even if a perfect WFC alignment correction is assumed. This is a natural consequence because the WFS signal is effectively an indication of the telescope optical performance and is not meant for fixing the M1 segment errors. The dynamic telescope pupil shape variation is the unique challenge that can be observed in this type of telescopes. This problem becomes important in the wavefront reconstruction. The use of Zernike polynomials in the reconstruction turned out to be ineffective due to the known higher-order aliasing and aberration coupling effects. Instead, we developed a feasible way of computing orthonormal slope polynomials for SH WFS analysis. This turned out to be extremely effective in the wavefront reconstruction and thus the alignment correction estimation. We plan to construct prototype wavefront sensors and perform extensive lab tests, characterization, and on-sky tests in the current HET before the WFU commissioning starts.

ACKNOWLEDGEMENTS

HETDEX is led by the University of Texas at Austin McDonald Observatory and Department of Astronomy with participation from the Universitäts-Sternwarte of the Ludwig-Maximilians-Universität München, the Max-Planck-Institut für Extraterrestriche-Physik (MPE), Astrophysikalisches Institut Potsdam (AIP), Texas A&M University, Pennsylvania State University, and the HET consortium. In addition to Institutional support, HETDEX is funded in part by gifts from Harold C. Simmons, Robert and Annie Graham, The Cynthia and George Mitchell Foundation, Louis and Julia Beecherl, Jim and Charlotte Finley, Bill and Bettye Nowlin, Robert and Fallon Vaughn, Eric Stumberg, and many others, by AFRL under agreement number FA9451-04-2-0355, and by the Texas Norman Hackerman Advanced Research Program under grants 003658-0005-2006 and 003658-0295-2007.

REFERENCES

[1] R. Savage, et al., "Current Status of the Hobby-Eberly Telescope wide field upgrade," Proc. SPIE, **7733**-149 (2010).

[2] G. J. Hill, et al., "The Hobby-Eberly Telescope Dark Energy Experiment," AIP Conference Proceedings, **773** 224-223 (2004).

[3] H. Lee, et al., "Metrology systems for the active alignment control of the Hobby-Eberly Telescope wide-field upgrade," Proc. SPIE, **7739**-28 (2010).

[4] P. Palunas, et al., "Imaging performance of the Hobby-Eberly Telescope," Proc. SPIE **6267**-127 (2006).

[5] M. T. Adams, et al., "Hobby-Eberly Telescope Segment Alignment Maintenance System," Proc. SPIE **4837,** 693-701 (2003).

[6] M. Hart, "Study and recommendation of wavefront sensing techniques for alignment of the Hobby-Eberly Telescope's HETDEX package," Internal Technical Report (June, 2008).

[7] J. N. Bahcall and R. M. Soneira, "The distribution of stars to V=16th magnitude near the north galactic pole – Normalization, clustering properties, and counts in various bands," Astrophys. J., **246**, 122-135 (1981).
[8] M. S. Bessel, "UBVRI photometry. II - The Cousins VRI system, its temperature and absolute flux calibration, and relevance for two-dimensional photometry," PASP, **91**, 589 (1979).
[9] M. S. Bessel, "VRI photometry - an addendum," PASP, **95**, 480 (1983).
[10] M. S. Bessel, "UBVRI passbands," PASP, **102**, 1181 (1990).
[11] D. S. Hayes and D. W. Latham, "A rediscussion of the atmospheric extinction and the absolute spectral-energy distribution of VEGA," Astrophys. J. **197**, 593 (1975).
[12] H. L. Johnson abd W. W. Morgan, "Fundamental stellar photometry for standards of spectral type on the revised system of the Yerkes spectral atlas," Astrophys. J. **117**, 313 (1953).
[13] ZEMAX: Software for optical system design, http://www.zemax.com/
[14] H. Lee, "Optical Programming Library in C and Fortran90: User's manual," (April, 2008).
[15] The OpenMP: API specification for parallel programming, http://openmp.org/wp/
[16] J. Herrmann, "Cross coupling and aliasing in modal wavefront estimation," J. Opt. Soc. Am. **71** 989-992 (1981).
[17] H. Lee, et al., "Orthonormal aberration polynominals for wavefront sensing over variable non-circular pupils of the Hobby-Eberly Telescope," Proc. SPIE, **7738**-59 (2010).
[18] H. Lee, "Use of Zernike polynomials for optimal estimation of orthonormal aberration coefficients over variable non-circular pupils," Optics Letters **35**, 2173-2175 (2010).
[19] H. Lee, et al., "Phase-retrieval analysis of the Hobby-Eberly Telescope primary mirror segment figure error," Proc. SPIE, **7738**-58 (2010).
[20] Schott, http://www.us.schott.com
[21] Daniel R. Neal, et al., "Shack-Hartmann wavefront sensor precision and accuracy," Proc. SPIE **4779** 148-160 (2002).